Cloud-radiative impact on the dynamics and predictability of an idealized extratropical cyclone

Behrooz Keshtgar[1], Aiko Voigt[2], Corinna Hoose[1], Michael Riemer[3], and Bernhard Mayer[4]

[1]Institute of Meteorology and Climate Research - Department Troposphere Research, Karlsruhe Institute of Technology, Karlsruhe, Germany
[2]Department of Meteorology and Geophysics, University of Vienna, Vienna, Austria
[3]Institute for Atmospheric Physics, Johannes Gutenberg-University Mainz, Mainz, Germany
[4]Meteorological Institute, Ludwig Maximilian University of Munich, Munich, Germany

Correspondence: Behrooz Keshtgar (behrooz.keshtgar@kit.edu)

Abstract. Extratropical cyclones drive midlatitude weather, including extreme events, and determine midlatitude climate. Their dynamics and predictability are strongly shaped by cloud diabatic processes. While the cloud impact due to latent heating is much studied, little is known about the impact of cloud radiative heating (CRH) on the dynamics and predictability of extratropical cyclones. Here, we address this question by means of baroclinic life cycle simulations performed at a convection-permitting resolution of 2.5 km with the ICON model. The simulations use a newly implemented channel setup with periodic boundary conditions in the zonal direction. Moreover, the simulations apply a new modeling technique for which only CRH interacts with the cyclone, which circumvents changes in the mean state due to clear-sky radiative cooling that has complicated the interpretation of previous work.

We find that CRH increases the kinetic energy of the cyclone system. The impact is most prominent at upper levels. To understand the CRH impact on the upper-tropospheric circulation, we diagnose the evolution of differences in potential vorticity between a simulation with and without CRH, and we quantify through which processes these differences grow over the course of the cyclone's life cycle. According to this diagnostic, CRH affects the cyclone mostly via the intensification of latent heating from cloud microphysical processes. Near the tropopause, direct diabatic modification of potential vorticity by intensified latent heat release precedes further changes in the tropopause by the upper-tropospheric divergent flow, which represents an indirect impact of latent heat release. Subsequently, differences in the tropopause structure amplify with the rotational flow during the highly nonlinear stage of the baroclinic wave.

Our results show that although CRH is comparably small in magnitude, it can affect extratropical cyclones by changing cloud microphysical heating and subsequently the large-scale flow. The CRH impact follows a previously identified mechanism of multi-stage upscale error growth. At the same time, simulations in which CRH is disabled after certain days show that the CRH impact operates throughout the entire intensification phase of the cyclone. This means that CRH does not merely provide an arbitrary initial perturbation to the cyclone, from which differences grow in a generic way. Instead, our results suggest that uncertainties associated with the representation of CRH in numerical models have a more systematic impact and may more fundamentally influence model predictions of extratropical cyclones.

1 Introduction

Extratropical cyclones are an essential component of the midlatitude circulation and determine midlatitude climate by transporting energy and moisture poleward. They also drive midlatitude weather and are responsible for extreme events such as strong windstorms and floods. Advances in understanding the dynamics of extratropical cyclones have led to better weather predictions (Schultz et al., 2019). While baroclinicity, i.e., horizontal gradients in temperature, is the main driver of extratropical cyclones (Catto, 2016), their dynamics and predictability are strongly affected by diabatic processes (Davis et al., 1993; Stoelinga, 1996). Work on diabatic impacts has mainly focused on latent heating, which is well known to amplify extratropical cyclones and modify their potential vorticity (PV) structure (Booth et al., 2013; Büeler and Pfahl, 2017). This includes studies of warm conveyor belts and the embedded latent heating, as well as the role of cloud microphysics (Joos and Wernli, 2012; Oertel et al., 2020).

In contrast, radiative processes have received much less attention. Several studies however showed that they should be considered more systematically. The cyclone case studies of Chagnon et al. (2013) and Spreitzer et al. (2019) highlighted the importance of longwave radiative cooling for the PV structure near the tropopause leading to a first-order impact on the amplitude evolution of the upper-tropospheric Rossby wave pattern (Teubler and Riemer, 2021). Baumgart et al. (2019) found radiation to be as important as other diabatic processes for forecast error growth on longer timescales, and Martínez-Alvarado et al. (2016) found that radiation contributes to the diabatic generation of forecast errors in warm conveyor belts and Rossby waves. Climate model studies showed that radiative processes from clouds shape the response of the extratropical circulation to increasing surface temperatures (Albern et al., 2019; Voigt et al., 2021). Although radiative heating and cooling in the atmosphere are smaller in magnitude than other diabatic processes, their persistence over longer periods of time can make them as important as other diabatic processes.

Many valuable insights on the role of latent heating were gained in idealized simulations of extratropical cyclones, i.e., so-called baroclinic life cycle simulations. To isolate the impact of latent heating, such simulations tend to neglect radiation altogether (e.g., Booth et al., 2013; Boutle et al., 2010; Tierney et al., 2018). Recently, Schäfer and Voigt (2018) were the first to show that radiation cuts the magnitude of idealized extratropical cyclone's strength in half, and that a substantial (although not the dominant) part of the radiative weakening was due to cloud-radiative processes. However, the dynamical mechanism by which radiation, and in particular cloud-radiative heating and cooling, affect cyclones has remained elusive from their work.

Radiative processes change the dynamics and physics of clouds (Klinger and Mayer, 2016). Spatial contrasts in radiative heating and cooling can destabilize clouds and their environment (Fu et al., 1995), thereby generating buoyancy that promotes cloud formation and enhances condensation. Tropical cyclone studies showed that cloud longwave absorption and emission by the anvil enhances upward motion and as a result, convective heating (Fovell et al., 2016), which Ruppert et al. (2020) found this effect to accelerate tropical cyclone development. Longwave radiation can also affect the microphysics of clouds, resulting in enhanced cloud droplet growth and an earlier formation of precipitation (Barekzai and Mayer, 2020).

It is also conceivable that cloud-radiation interaction might affect the predictability of extratropical cyclones. Given the multiscale nature of the atmosphere, small errors on the grid-scale associated with physical processes can grow to the synoptic-

scale, resulting in substantial forecast errors (e.g. Zhang et al., 2007; Baumgart et al., 2019). The cyclone case studies of Joos and Forbes (2016) showed that changes in the microphysical parameterization affect the outflow of warm convey belts and

60 thereby the evolution of the upper-tropospheric flow. Cloud-radiative processes might act as a similar source of forecast error, but this possibility has not been addressed so far.

In this study, we conduct idealized baroclinic life cycle simulations with a convection-permitting resolution of 2.5 km to provide the first systematic investigation of cloud-radiative impact on extratropical cyclones. The high resolution allows the model to treat deep convection explicitly, i.e., no deep convection scheme needs to be used and clouds and updrafts interact

65 directly. Using these simulations, we address three research questions:

- How strongly do cloud-radiative heating affect extratropical cyclones?

- What are the mechanisms that underlie the cloud-radiative impact?

- What does this imply for the impact of cloud-radiation on cyclone predictability?

The paper is organized as follows. The model setup and simulation design are described in section 2. Section 3 characterizes
70 the cloud-radiative impact on the baroclinic life cycle in terms of the cyclone strength and PV. In section 4, we use a PV-difference diagnostic to understand how cloud-radiative heating and cooling change the dynamics and evolution of the cyclone. In section 5, we assess the cloud-radiative impact on cyclone predictability by disabling cloud-radiation interaction at a number of days during the cyclone growth. Finally, the paper closes with the conclusion in section 6.

2 Methods

75 This section describes the model setup that we use for the baroclinic life cycle simulations, and introduces the new modeling approach that we have developed to study the impact of cloud-radiative heating (CRH). We note that in this paper, the CRH term refers to both cloud-radiative heating and cooling.

2.1 ICON model setup

We use the ICOsahedral Nonhydrostatic atmosphere model (ICON-NWP, version 2.6.2.2; Zängl et al. (2015)). For the simula-
80 tions, we use a limited-area channel setup on a Cartesian f-plane with periodic boundary conditions in zonal direction and fixed meridional boundaries. Because a channel setup was not available by default in ICON, we introduced a new grid by building upon the planar-channel grid available for the ICON ocean component and the torus grid available in the ICON atmosphere component.

The channel setup allows for high horizontal resolution while keeping computational costs manageable for more simulations.
85 Another advantage is its perfectly uniform grid, i.e., each triangular grid cell has exactly the same area. We use a convection-permitting resolution of 2.5 km in the horizontal direction which results in nearly 6 million grid points. In the vertical direction, we use 70 model levels. The Coriolis parameter is constant with a value for 45 degrees north. For the domain size, we set

the channel width to 9000 km and the channel length to 4000 km, which approximately equals 81 degrees in latitudinal and

51 degrees in longitudinal direction. The large meridional extent ensures that the simulated cyclone is not influenced by the

90 North-South boundaries. Test simulations showed that the cyclone is sensitive to the domain length. For smaller lengths, the

cyclone is rather weak, while for larger lengths it becomes very strong. We thus settled for a domain length of 4000 km.

The model surface is specified as an ice-free ocean surface with no topography and time-constant sea surface temperatures

that are 0.5 K cooler than the initial temperature of the lowest model level. The model is run with full physics including the

shallow convection scheme of Bechtold et al. (2008) and the turbulence scheme of Raschendorfer (2001). The deep convection

95 scheme is disabled. Cloud microphysics and grid-scale precipitation are represented by the two-ice-category one-moment

scheme of Doms et al. (2011). Longwave and shortwave radiation are calculated with the Rapid Radiative Transfer Model

(Mlawer et al., 1997). The diurnal cycle is retained and equinox conditions for the shortwave radiation calculation are used.

The initial conditions are the same as in Schäfer and Voigt (2018) and follow the life cycle type 1 configuration of Polvani

and Esler (2007). The relative humidity is set to 80%. With the initial wind profile being baroclinically unstable, the baroclinic

100 life cycle is triggered by adding a sinusoidal thermal wave with a 1 K amplitude at all levels and with a wavelength equal to the

domain length. This means that a single cyclone is simulated, instead of a train of six cyclones as in Schäfer and Voigt (2018).

The configuration results in a reasonable cyclone whose structure is typical for wintertime extratropical cyclones. This is

illustrated in Fig. 1, which shows the spatial distribution of surface pressure, cloud cover, and precipitation rate for a cyclone

simulated without radiation. For visualization and remapping purposes, the map plots in our paper use the geographical latitude

105 and longitude coordinates that are assigned to grid cells during the grid generation according to the Cartesian length and width

of the domain. Yet, the model computation is solely based on the Cartesian grid.
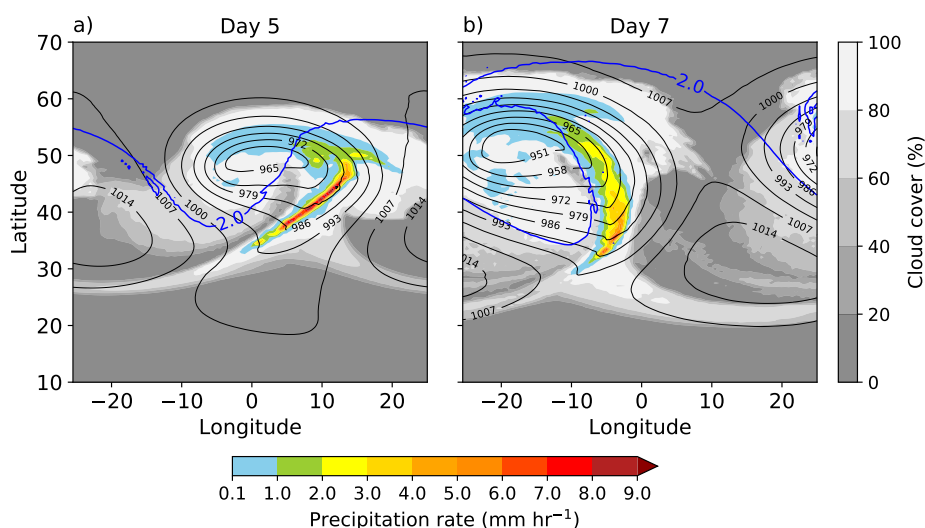
Figure 1. Surface pressure (black contours), total precipitation rate (colors), and cloud cover (gray shadings) for the cyclone simulation without radiation at (a) day 5 and (b) day 7. The blue lines indicate the dynamical tropopause as given by the 2 PVU contour on the 326 K isentrope.

The region with the highest precipitation marks the position of the warm conveyor belt, which is located east of the cyclone center in Fig. 1 a. The warm conveyor belt moves ahead of the cold front and splits into two branches. One branch wraps cyclonically north of the cyclone center, and the other one anticyclonically towards the high-pressure region (Fig. 1 a). The cloud-free region just behind the warm conveyor belt marks the location of the descending cold, dry air. From the southwest of the cyclone center to the high-pressure center, shallow stratocumulus clouds form due to the passing of cold air over the warm sea surface.

Using Cartesian instead of spherical coordinates that had been used in the global setup of Schäfer and Voigt (2018), results in a different, but no less realistic cyclone structure. It is well known that baroclinic waves simulated on a Cartesian geometry display stronger cyclonic flows and upper cyclonic wave-breaking during their mature phase. This is evident from the evolution of the dynamical tropopause in Fig. 1 b, which shows that the tropopause wave rolls up cyclonically, exhibiting characteristics of the cyclonic life-cycle paradigm of Thorncroft et al. (1993). Similar behavior can be achieved for a spherical geometry by adding a small cyclonic shear to the initial jet. More information on the impact of geometries on the baroclinic life cycle can be found in Balasubramanian and Garner (1997).

2.2 Simulation design

We develop and apply a new modeling approach that isolates the impact of cloud radiation from that of clear-sky radiation in a clean manner. This approach is needed since when radiation is included in baroclinic life cycle simulations, Schäfer and Voigt (2018) found a strong atmospheric cooling in the first days. This initial cooling is reproduced for our model setup in Fig. 2 a. When radiation is active, the atmospheric state changes substantially before the cyclone starts to form, which complicates the comparison of simulations with and without radiation.

Our approach removes the initial radiative adjustment so that the cyclone forms in nearly the same background state independent of whether CRH is active or not. This is shown in Fig. 2 b and c. We achieve this by only feeding the cloud-related part of radiative heating to the dynamical core while ignoring the clear-sky contribution. The cloud-related part is defined as the all-sky minus the clear-sky radiative heating rates. In terms of the thermodynamic equation, our approach is described by

$$c_p \frac{dT}{dt} - \frac{1}{\rho} \frac{dp}{dt} = (RAD_{all-sky} - RAD_{clear-sky}) + J, \tag{1}$$

where J represents the heating rates from other diabatic processes. In terms of model implementation, our approach requires two calls to the radiation scheme, one with clouds and one with clouds set to zero.

To study to what extent the cloud-radiative impact is linear, we perform an additional simulation in which we multiply CRH by a factor of two before feeding it to the dynamical core (cf. Eq. 1). This simulation will be referenced as 2xCRH in the following. For convenience, from now on the simulations without radiation and with cloud radiation will be referenced as REF and CRH, respectively.
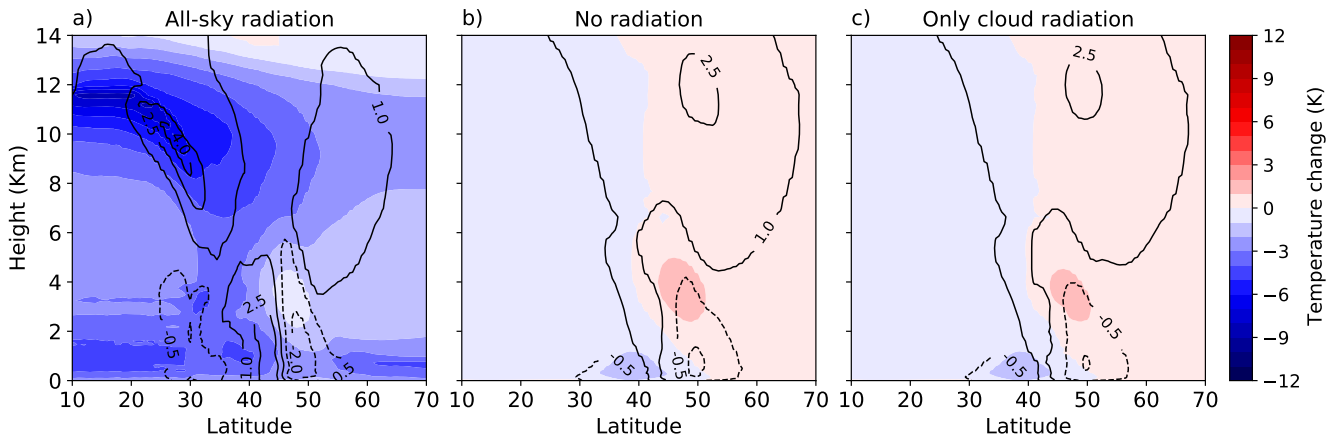
Figure 2. Zonal-mean changes in temperature and zonal wind at day 3 for simulations with (a) all-sky radiation, (b) no radiation, and (c) cloud radiation only.

For the analysis, we use the Climate Data Operators (Schulzweida, 2019) and first remap the model output from the triangular grid to a regular rectangular grid with the same resolution using the nearest neighbor interpolation method. We then interpolate the data to a 0.5 deg x 0.5 deg latitude-longitude grid using conservative interpolation.

3 Cloud radiative impact on the cyclone

In this section, we assess the impact of CRH on the evolution of the baroclinic life cycle. To this end, we compare the REF simulation with the simulations that include CRH as given by Eq. 1.

3.1 Cyclone intensity

We characterize cyclone intensity by means of eddy kinetic energy and cyclone center pressure. Eddy kinetic energy is calculated with respect to the deviation from the zonal-mean wind field at each time step. Cyclone central pressure is simply given by the minimum surface pressure within the model domain. Fig. 3 shows the time evolution of the intensity metrics for the simulations REF, CRH, and 2xCRH.

According to the cyclone central pressure shown in Fig. 3 a, cyclone development starts at around day 3 and peaks at around day 7. CRH has no noticeable impact on cyclone development as measured by the central pressure. However, CRH clearly strengthens the cyclone in terms of eddy kinetic energy. When CRH is taken into account, eddy kinetic energy increases after day 6 compared to the REF simulation, signaling a stronger cyclone whose peak intensity is delayed. The cloud-radiative impact is more prominent at upper levels, and weaker at lower levels (cf. Fig. 3 b and c). This implies that CRH mostly influences the near-tropopause flow. Doubling CRH in the 2xCRH simulation further increases eddy kinetic energy, although the change between the CRH and 2xCRH simulations is smaller than that between the REF and the CRH simulations (Fig. 3 b).
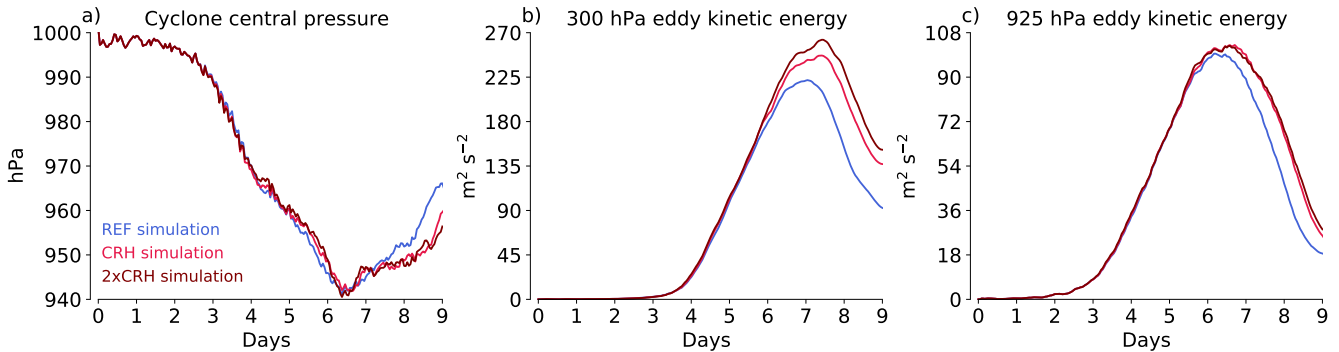
Figure 3. Evolution of (a) cyclone central pressure and eddy kinetic energy at (b) 300 hPa and (c) 925 hPa for simulations with no radiation (REF), cloud-radiative heating (CRH), and cloud-radiative heating increased by a factor of 2 (2xCRH).

155   Our results are in contrast to the global simulations of Schäfer and Voigt (2018), who reported that CRH weakens cyclones. In a related study that is in preparation, we have found that the results of Schäfer and Voigt (2018) are sensitive to the ICON version. When repeating their global simulations with ICON version 2.6.2.2 instead of version 2.0.15, CRH leads to a stronger cyclone, in agreement with our channel setup. This shows that model differences in clouds and their radiative heating can modulate the cloud-radiative impact in important ways that are not understood. Here, however, we focus on the underlying

160   dynamics of CRH impact as represented in our simulations and modeling setup.

In conjunction with the cyclone intensity metrics, Fig. 4 shows the evolution of total precipitation rate and cloud cover for the three simulations and the differences with respect to the REF simulation. Precipitation starts to form around day 3 and peaks at day 6.5 for all simulations (Fig. 4 a). Total cloud cover increases constantly during the 9 days of the simulation. When CRH is active, total precipitation rate and total cloud cover increase compared to the REF simulation (Fig. 4 a and b). Similar

165   to the eddy kinetic energy (Fig. 3), the CRH impact gets stronger with amplified CRH.
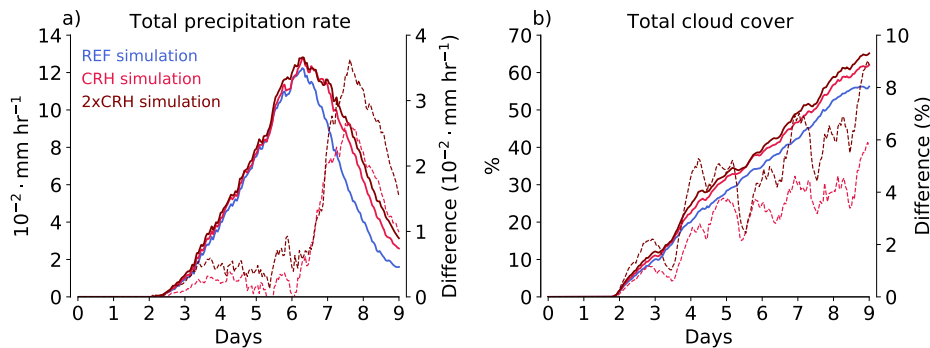
Figure 4. Time evolution of (a) total precipitation rate and (b) total cloud cover for different treatments of cloud-radiative heating. The dashed lines denote the difference of the CRH and 2xCRH simulations with respect to the REF simulation. For the differences, the right y-axis is used.

The CRH-induced increase in precipitation indicates that the cloud-radiative impact might operate via changes in condensation and latent heating, which are known to strongly affect cyclone development. In the following subsection, we will indeed look at this point in more detail by analyzing the PV evolution.

3.2 Cloud-radiative impact on potential vorticity

170 PV combines dynamic and thermodynamic information and is a conserved quantity for frictionless adiabatic flow. Therefore, PV can serve as a tracer that indicates how the circulation is modified by diabatic processes (e.g. Joos and Wernli, 2012). In addition, the PV distribution on isentropic surfaces helps to characterize the synoptic-scale structure of baroclinic waves and their propagation (Hoskins et al., 1985).

The first row in Fig. 5 shows the evolution of PV at the 326 K isentrope for the REF simulation. This isentropic level includes
175 tropospheric air at lower latitudes and stratospheric air at higher latitudes. The tropopause is located in a region of strong PV gradient that separates tropospheric from stratospheric air masses. The dynamical tropopause is shown by the 2 PVU contour and its wave-like distortion and eventual breaking can be used to depict the development of the cyclone.

Similar to eddy kinetic energy, the wave amplitude starts to grow at around day 3 and reaches its maximum at day 7 with impending wave breaking. The wave breaking is evident from the reversal of the PV meridional gradient in the eastern part of
180 the domain at day 7 (Fig. 5 c). This is followed by the decay phase of the wave through barotropic conversion of eddy kinetic energy into zonal-mean kinetic energy (not shown).

To demonstrate the impact of CRH on the evolution of PV, the differences of PV between the CRH and the REF simulations are plotted at upper and lower levels in the second and third rows of Fig. 5, respectively. At the upper levels shown by the 326 K isentrope, PV differences at days 5 and 6 are small and limited to regions close to the dynamical tropopause (Fig. 5 e and f),
185 but grow to substantial values at days 7 and 8 (Fig. 5 g and h). At the lower levels shown by the 925 hPa isobaric surface, PV differences are located near the cyclone center and in the warm conveyor belt, however, they are comparably small throughout the entire simulation.

The distribution of positive and negative PV differences at upper levels indicates that CRH slows the propagation of the baroclinic wave towards the east, thereby postponing the cyclonic wave-breaking, and it increases the wave amplitude. These
190 impacts can be seen from the deformation of the dynamical tropopause wave at days 7 and 8 (Fig. 5 g and h). Higher PV east of the trough center and lower PV at the tip of the ridge for the REF simulation at day 7 indicate an earlier wave-breaking and termination of the wave intensification. Positive PV differences west of the trough center and negative PV differences on the poleward side of the ridge (Fig. 5 g and h) indicate a deeper tropopause fold and stronger ridge for the baroclinic wave with CRH.

195 The CRH impact is consistent with the diabatic intensification of baroclinic waves in terms of wave amplitude and growth rate. For instance, Chagnon et al. (2013) showed in their cyclone case study that the PV anomalies generated by diabatic processes help to keep the upper level PV wave phase-locked with the surface potential temperature wave. That means that each wave component will help to increase the amplitude of the other. This mutual interaction then slows down the eastward propagation of the wave and amplifies the growth rate. Thus, including CRH helps to reinforce this impact, resulting in higher

200 intensity and delayed intensity peak time. Overall, the evolution of PV is consistent with that of eddy kinetic energy and the stronger impact of CRH at upper levels.
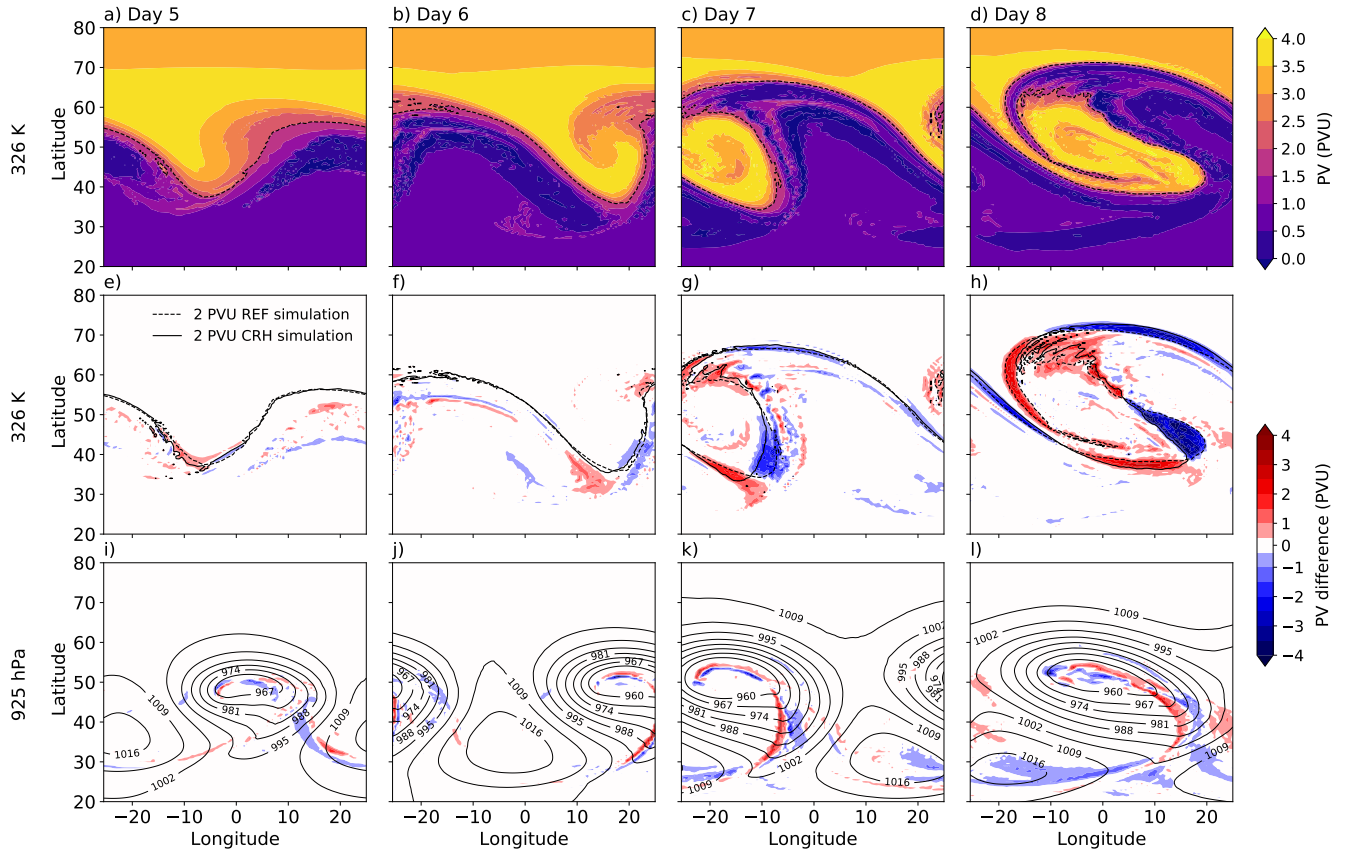
Figure 5. Upper level PV evolution on the 326 K isentrope for the REF simulation from days 5 to 8 (a-d). PV differences between the CRH and REF simulations (CRH-REF) at upper levels on the 326 K isentrope (e-h) and at lower levels on the 925 hPa isobaric surface (i-l). The dynamical tropopause is shown in solid and dashed black lines for CRH and REF simulations respectively. Thin black contours depict the mean surface pressure between the two simulations.

3.3 Potential vorticity tendency from diabatic processes

We now investigate the modification of PV by diabatic processes and the relation to the PV differences diagnosed in Sect. 3.2. Diabatic processes can modify the near-tropopause PV and hence the tropopause structure. The impact can be direct through 205 diabatically generated PV anomalies, most notably as the result of vertical gradients in diabatic heating, or indirect through changes in wind and PV advection.

We start with the diabatic PV tendencies of Ertel's PV (Ertel, 1942):

$$PV = \frac{1}{\rho}\eta \cdot \nabla\theta. \tag{2}$$

For a non-conservative flow, the diabatic modification of PV is given by (e.g., Joos and Wernli, 2012):

210
$$\frac{D}{Dt}PV = \frac{1}{\rho}\eta \cdot \nabla\dot{\theta} \approx \frac{1}{\rho}\eta_z \cdot \frac{\partial}{\partial z}\dot{\theta}. \tag{3}$$

$\frac{D}{Dt}$ denotes the material derivative, ρ is the density, η is the absolute vorticity vector, and $\dot{\theta}$ is the diabatic heating tendency. The modification of PV by frictional forces is neglected here[1]. The approximation for the r.h.s. of Eq. 3 makes the assumption that the vertical gradient of $\dot{\theta}$ dominates the PV tendency, which is typically justified. The main effect of diabatic heating is, therefore, the increase of PV below the maximum of the heating and the reduction of PV above it. For our analysis, we derive

215 the diabatic PV tendencies on model levels to benefit from the available high vertical resolution.

The overwhelming part of the heating from cloud-radiation-interaction and cloud microphysics occurs within the warm conveyor belt of the cyclone, which is characterized by extensive cloud formation and heavy precipitation. For the simulation with CRH, Fig. 6 shows cross-sections through the warm conveyor belt for cloud cover, CRH, and microphysical heating at day 5.5. The figure also shows the associated diabatic PV tendencies.

220 The two cloud bands mark the regions of ascent in the warm conveyor belt and the cyclonic branch that is located further north (Fig. 6 a). In these regions, longwave CRH leads to strong cooling near the cloud top and modest warming below (Fig. 6 b). In contrast, shortwave CRH warms the top of the clouds and weakly cools the cloud layer below (Fig. 6 c). Compared to longwave CRH, shortwave CRH is small and is limited mostly to near the cloud top.

A substantial part of diabatic heating in these cloudy regions is associated with cloud microphysical processes (Fig. 6 d).
225 Strong microphysical heating occurs inside the cloud bands, with some cooling below. Joos and Wernli (2012) showed in their warm conveyor belt case study that the largest contribution to microphysical heating is due to condensation of water vapor and the depositional growth of snow, and that cooling is mostly due to the evaporation of the rain and snow melting.

The vertical gradients in CRH and microphysical heating lead to diabatic PV increase and reduction according to Eq. 3 as shown in panels e, f, and g of Fig. 6. Longwave CRH mostly generates a vertical dipole of negative and positive PV
230 tendencies near the cloud top (Fig. 6 e). For shortwave CRH, the dipole is reversed and somewhat compensates for the longwave CRH impact. Consistent with the larger heating rates, PV tendencies associated with cloud microphysical processes are much stronger.

The relationship between cloud diabatic heating and the associated PV tendencies is further illustrated in Fig. 7, which shows the vertical profiles of heating rates and PV tendencies integrated spatially over the entire domain and averaged between days
235 5 to 8. For comparison, the microphysical heating and its PV tendency for the REF simulation are also plotted by the dashed lines.

---

[1]Frictional forces are included in Sect. 4, where they are found to be small during the growth phase of the cyclone.

On average, Longwave CRH leads to a noticeable cooling at upper levels. In the boundary layer, however, longwave CRH cools the boundary layer top and warms the layer from below (Fig. 7 a). Cloud microphysical processes on the other hand produce a much stronger heating at mid-levels between 4-6 km (Fig. 7 a).
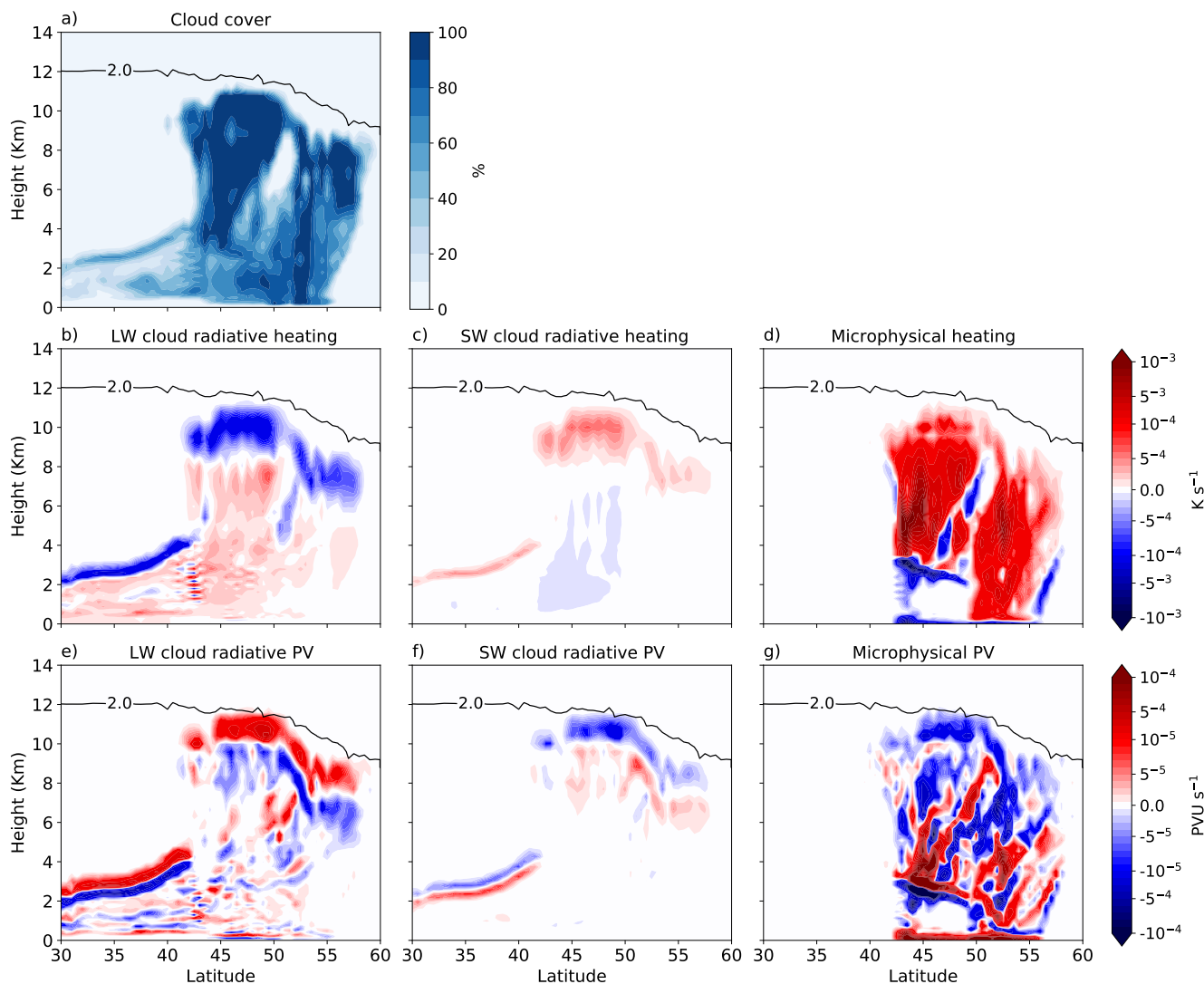
Figure 6. Cross-section through the warm conveyer belt at day 5.5 for the simulation with CRH. (a) cloud cover, (b) longwave CRH, (c) shortwave CRH, and (d) heating from cloud microphysical processes. Panels (e), (f), and (g) show the associated diabatic PV tendencies.

240   Previous studies showed that the vertical dipole of PV tendencies associated with cloud microphysical heating (Fig. 7 b, dark red line) help to increase the intensity of the cyclone (Stoelinga, 1996; Büeler and Pfahl, 2017). At lower levels, positive PV tendencies tend to form and increase the lower-tropospheric PV. The negative PV tendencies above the maximum microphysical

heating lead to the downstream upper level ridge amplification. This configuration supports the typical westward tilt between lower and upper level waves, hence cyclone intensification.

245   PV tendencies by CRH may enhance or weaken the aforementioned PV tendencies associated with cyclone intensification. Positive PV tendencies by longwave CRH at upper levels reduce the net negative PV tendency. but, at lower levels between 2-4 km, they tend to interfere positively to increase PV (Fig. 7 b). However, CRH also amplifies the microphysical heating and its PV tendency dipole (Fig. 7 a and b). This is related to the destabilization of the ascent region within the cyclone by longwave CRH dipole (Fig. 6 b). Cloud top cooling and warming below increase the buoyancy of the layer leading to stronger ascending

250   motion and heating. The stronger microphysical PV tendency dipole is in favor of cyclone intensification and hence higher eddy kinetic energy.
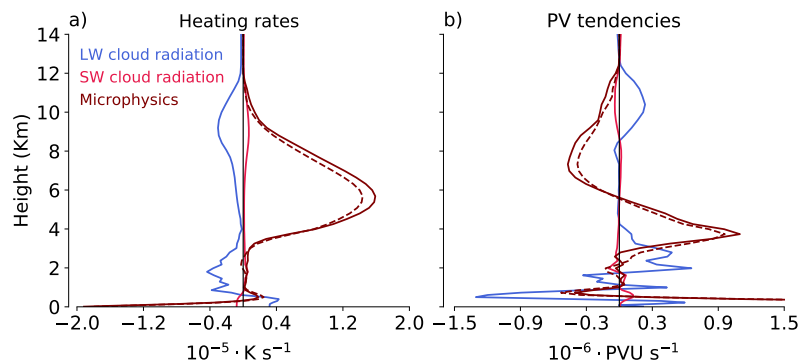
Figure 7. Vertical profiles of spatially integrated (a) cloud radiative and microphysical heating rates averaged between days 5 to 8. Panel (b) demonstrates the associated PV tendencies. The dashed lines depict the profiles in the REF simulation.

Moreover, the dipole of positive and negative PV tendencies by CRH in the boundary layer (Fig. 7 b) suggests that the layer becomes even more turbulent. Thus, CRH can impact not only the microphysical processes but also other diabatic processes. To demonstrate how CRH affects diabatic PV tendencies, Fig. 8 shows the evolution of spatially integrated PV tendencies from

255   individual diabatic processes. Besides cloud-radiative heating, the latter includes the heating rates from turbulence, convection, cloud microphysics and saturation adjustment. Cloud microphysics and saturation adjustment are summed up to the total latent heating. The PV tendencies are shown at four layers to characterize their variation with height and are shown for the CRH stimulation in the first row and their differences with the REF simulation in the second row.

At upper levels (10-12 km) all diabatic processes generate negative PV tendencies except longwave CRH, which damps the

260   net negative diabatic PV tendency (Fig. 8 a). At mid-levels (6-8 Km) a strong negative PV tendency by total latent heating drives the total diabatic PV tendency (Fig. 8 b). However, at lower levels (2-4 km) and in the boundary layer (0-2 km), total diabatic PV tendencies are controlled by opposing impacts from latent heating and turbulence (Fig. 8 c and d). The PV tendencies associated with convection are small since deep convection is resolved in our simulations and noticeable values appear only in the boundary layer due to parameterized shallow convection.

265   When CRH is included, the PV generation from latent heating and turbulence changes at all levels. This is shown in the
lower row of Fig. 8. In fact, the PV tendencies associated with turbulence and total latent heating are amplified at all levels in
the CRH simulation compared to the REF simulation. At upper levels, however, this amplification is more than compensated by
the strong positive PV tendency from longwave CRH (Fig. 8 e). At mid levels, the dominating negative PV tendency from total
latent heating becomes even more negative when CRH is included. At lower levels, the inclusion of CRH has the strongest
270 impact on the diabatic PV tendencies from latent heating and turbulence, although the net change in the overall diabatic
PV tendency is small as turbulence and latent heating largely compensate each other. A similar compensation occurs in the
boundary layer, where noticeable differences in the total diabatic PV tendency between the simulations with and without CRH
occur only after the cyclone has reached peak intensity.
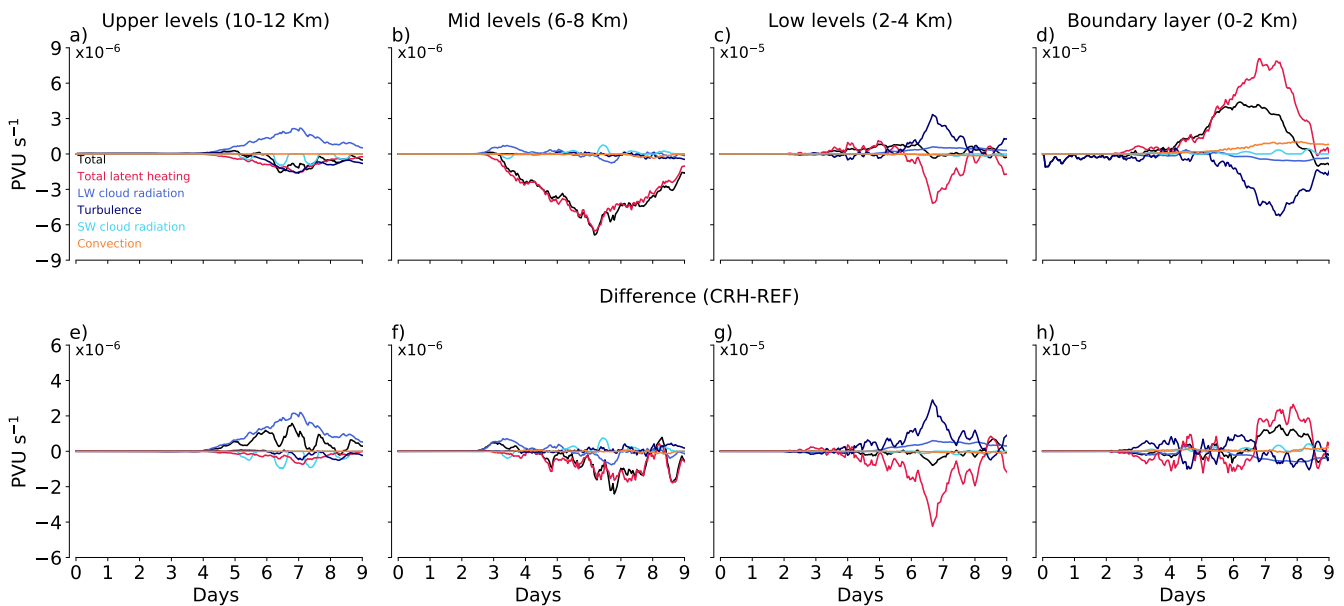
Figure 8. Time evolution of spatially integrated diabatic PV tendencies accumulated between (a) 10-12 km, (b) 6-8 km, (c) 2-4 km, and (d)
0-2 km for CRH simulation. Panels (e-h) show the diabatic PV differences between the CRH and REF simulations (CRH-REF). Note the
different scales in panels.

    During the cyclone maximum intensity phase, most of the PV anomalies are controlled by diabatic processes at lower levels
275 (Büeler and Pfahl, 2017). Thus, small changes in the net diabatic PV tendency at lower levels and boundary layer due to
compensation between amplified turbulence and latent heating PV tendencies might explain the weak impact of CRH on the
eddy kinetic energy at 925 hPa found in Fig. 3 c. Near the tropopause, however, PV is strongly controlled by PV advection
from the rotational and divergent flow (Chagnon et al. (2013), Riemer and Jones (2010)) so that changes in the diabatic PV
tendencies near the tropopause may not fully explain the PV differences shown in Sect. 3.2. Therefore, we study the impact of
280 CRH on advective terms and their relation to the PV differences in more detail in the following section.

4 Understanding the cloud-radiative impact by diagnosing the growth of PV differences

The previous sections have documented a clear impact of CRH on the idealized cyclone and the evolution of PV. To understand the underlying dynamical mechanisms, we now compare the simulations with and without CRH by means of the PV error growth framework of Baumgart et al. (2018, 2019).

4.1 Diagnostic framework and application to our simulations

The framework of Baumgart et al. (2018, 2019) has been developed to understand the growth of PV forecast errors near the tropopause in numerical weather predictions at the synoptic-scale. The framework has led to important insights into the dynamics and multiple scales of the error growth from the convective to the synoptic or even hemispheric scale. To this end, the framework compares the near-tropopause PV tendencies between a reference analysis and a forecast simulation and quantifies the adiabatic and diabatic mechanisms that lead to the PV error growth in the forecast.

Here, we apply the framework by considering the REF simulation without radiation as the reference analysis, and the CRH simulation as the forecast. Because a "true" evolution of the idealized cyclone does not exist, we use the terminology of "difference" instead of "error" in the following.

We follow the approach described in Baumgart et al. (2019) for deriving the PV tendency and its decomposition, apart from small changes that are described below. On isentropic levels, Ertel PV tendency is given by

$$\frac{\partial PV}{\partial t} = -\mathbf{v} \cdot \nabla_\theta PV - \dot{\theta}\frac{\partial PV}{\partial \theta} + PV\frac{\partial \dot{\theta}}{\partial \theta} + \frac{1}{\sigma}\mathbf{k} \cdot (\nabla \times \dot{\mathbf{v}}) + RES. \tag{4}$$

The first term on the r.h.s accounts for the PV tendency due to advection, and the remaining terms are the PV tendencies due to diabatic processes. The residual term RES arises from processes that can not be quantified with the available model output (e.g., numerical diffusion), from numerical errors due to the spatial and temporal discretization, and from the interpolation of model output. $\mathbf{v}$ is the horizontal wind and ∇ is the horizontal gradient, which are both calculated on isentropic levels. $\dot{\theta}$ is the diabatic heating. $\dot{\mathbf{v}}$ is the diabatic horizontal wind tendencies. Our analysis includes all diabatic heating tendencies of the ICON model as well as the diabatic wind tendencies due to the parameterization of turbulence, shallow convection and non-orographic gravity waves.

To account for different mechanisms involved in the evolution of PV near the tropopause, the horizontal wind in Eq. 4 can be partitioned into contributions from rotational and divergent winds by means of Helmholtz decomposition,

$$\mathbf{v} = \mathbf{v}_{rot} + \mathbf{v}_{div}. \tag{5}$$

The rotational wind accounts for advective PV tendency by the (quasi-barotropic) near-tropopause flow and by the winds associated with the low-level PV anomalies (i.e, baroclinic interaction). The divergent wind contains a contribution associated with dry (balanced dynamics) and one associated with moist dynamics, mostly the invigoration of upper-tropospheric divergence

by latent heat release below. In the presence of prominent latent heat release, which is the case in our experiments, several case studies have indicated that PV advection near the tropopause by the divergent wind can be interpreted to a large extent as an indirect impact of moist processes (see, e.g., discussion and references in Teubler and Riemer, 2021). We here adapt the interpretation that the divergent term is predominantly associated with changes in diabatic heating. Baumgart et al. (2018) showed that the contribution of the lower-level winds to near tropopause PV error growth is on average small. Because the differences of the cyclone PV evolution in our experiments are relatively small at low levels, we restrict ourselves to a Helmholtz decomposition and avoid in the current study the intricateness of piecewise PV inversion.

Our aim is to understand how CRH affects the cyclone and PV relative to the cyclone without radiation. We therefore focus on the PV difference between the REF and CRH simulations,

$$\Delta PV = PV_{\text{REF}} - PV_{\text{CRH}}. \tag{6}$$

Again following Baumgart et al. (2019), we consider the spatial integration of the squared PV difference over a fixed domain A and refer to this as the difference potential enstrophy ($\mathscr{PV} = \frac{(\Delta PV)^2}{2}$). The difference potential enstrophy tendency is then given by

$$\frac{d\mathscr{PV}}{dt} = \frac{1}{A}\int_A \frac{\partial}{\partial t}\frac{(\Delta PV)^2}{2}dA. \tag{7}$$

We calculate the time derivative in Eq. 7 by centered finite difference method. Based on the PV tendency equation (Eq. 4) and the Helmholtz decomposition (Eq. 5), the difference potential enstrophy tendency can then be decomposed into different processes:

$$\frac{d\mathscr{PV}}{dt} = \mathscr{PV}_{rot} + \mathscr{PV}_{div} + \mathscr{PV}_{dia} + RES, \tag{8}$$

where

$$\mathscr{PV}_{rot} = \frac{1}{A}\int_A -\Delta PV\Delta\mathbf{v}_{rot}\cdot\nabla_\theta\overline{PV}dA,$$

$$\mathscr{PV}_{div} = \frac{1}{A}[\int_A -\Delta PV\Delta\mathbf{v}_{div}\cdot\nabla_\theta\overline{PV}dA + \int_A \frac{(\Delta PV)^2}{2}\nabla_\theta\cdot\overline{\mathbf{v}}_{div}dA],$$

$$\mathscr{PV}_{dia} = \frac{1}{A}\int_A \Delta PV[-\Delta\dot\theta\frac{\partial\overline{PV}}{\partial\theta} - \bar{\bar\theta}\frac{\partial\Delta PV}{\partial\theta} + \Delta PV\frac{\partial\bar{\bar\theta}}{\partial\theta} + \overline{PV}\frac{\partial\Delta\dot\theta}{\partial\theta}$$

$$+\frac{1}{\bar\sigma}\mathbf{k}\cdot(\nabla\times\Delta\dot{\mathbf{v}}) + \frac{1}{\Delta\sigma}\mathbf{k}\cdot(\nabla\times\overline{\dot{\mathbf{v}}})]dA. \tag{9}$$

330 The Δ symbol indicates the difference of a variable between the CRH and REF simulations, whereas the overbar means that the variable is averaged between the CRH and REF simulations. $\mathscr{PV}_{rot}$ and $\mathscr{PV}_{div}$ measure the contributions from advection by the rotational and divergent wind, respectively. The contributions from parametrized diabatic heating and wind tendencies are given by $\mathscr{PV}_{dia}$. For reference, the above equation is the same as Eq. 9 of Baumgart et al. (2019).

To compute Eq. 8 we linearly interpolate the model output from height-based model levels to isentropic levels that intersect
335 the midlatitude tropopause. We choose the 326 K isentrope for the analysis and compute Eq. 8 on a 1 deg x 1 deg grid. We have tested at which spatial resolution the diagnostic is best used. The tests were necessary because our high-resolution simulations exhibit a lot of small-scale PV structures that could substantially affect the budget in Eq. 8. Results showed that interpolating to the 1 deg x 1 deg grid leads to the best results. In fact, when we computed Eq. 8 for a spatial resolution close to the 2.5 km resolution of the model, Eq. 8 is not even approximately closed. This happens because of strong co-variability between PV and
340 diabatic heating on small scales, which leads to large diabatic tendencies. However, this small-scale co-variability is short-lived and hence in our view is not necessarily relevant for the synoptic-scale dynamics that we are interested in. We also note that Baumgart et al. (2019) developed and tested the diagnostics for the synoptic-scale.

Still, also on the 1 deg x 1 deg grid, Eq. 8 is not perfectly closed. In the early stages, the difference potential enstrophy tendency on the l.h.s is larger than the sum of the individual terms on the r.h.s. This is likely due to errors in the spatial
345 discretization. Shortly before the cyclone reaches maturity and thereafter, the l.h.s. of Eq. 8 becomes smaller than the r.h.s. It is most reasonable to assume that this is due to a sink of difference potential enstrophy from model diffusion, discussed in detail in Baumgart et al. (2018). This sink cannot be quantified from our model output and means that in the presence of appreciable PV differences one should in fact not expect a perfectly closed budget. The generation of PV anomalies by a numerical model's dynamical core has been demonstrated also in (e.g., Saffin et al., 2016). Nevertheless and despite these limitations, the r.h.s. of
350 Eq. 8 captures the evolution of difference potential enstrophy tendency reasonably well.

4.2 Evolution of difference potential enstrophy

Before studying the domain integral, we look into the spatial distribution of the different contributions to the difference potential enstrophy tendency. These are shown in Fig. 9 for day 7.5, i.e., the time of maximum intensity of the cyclone.

Similar to the near-tropopause PV differences studied in Sect. 3, difference potential enstrophy and its contributions attain
355 their largest values along the dynamical tropopause (Fig. 9). The diabatic tendencies are small and of noticeable magnitude only in the trough region (Fig. 9 b). A further decomposition of the diabatic tendencies shows that they are dominated by total latent heating and CRH (not shown). The differences associated with CRH are mostly located in the ridge whereas differences by total latent heating are located in the trough region (not shown).

Indeed and as expected at this stage of the cyclone life cycle, advective tendencies dominate the differences in the near-
360 tropopause PV (Fig. 9 c and d). The rotational contribution is somewhat larger than the divergent contribution, but both are important. This result is consistent with previous findings that on synoptic-scales differences in the PV evolution are governed by balanced dynamics and that the rotational tendency associated with non-linear Rossby wave dynamics controls the near-tropopause PV gradient. (Baumgart et al., 2018).
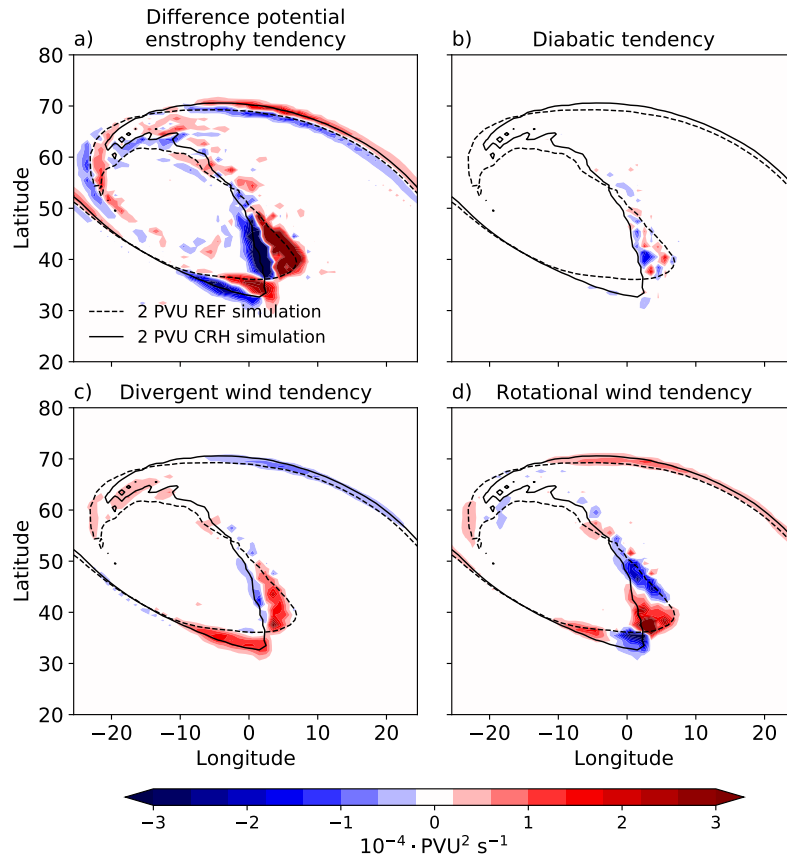
Figure 9. Spatial distribution of (a) difference potential enstrophy tendency and contributions from (b) diabatic processes as well as advection by the (c) divergent flow and (d) the rotational flow at day 7.5. The black contours denote the dynamical tropopause for the cyclone with (solid) and without CRH (dashed) on the 326 K isentrope.

To show how different processes contribute to the evolution of difference potential enstrophy, we consider the time series of
365 spatially integrated tendencies. These are plotted in Fig. 10. Although Eq. 8 is not perfectly closed for the reasons explained in Sect. 4.1., the sum of the diagnosed contributions (cyan line) matches the actual difference potential enstrophy tendency (black line) reasonably well.

Until day 6 the contribution from diabatic processes is almost in the same range as that from advection. However, close to the cyclone mature stage between days 6 to 8, the growth of difference potential enstrophy is dominated by advection, whose
370 impact via the divergent and rotational flow is one order of magnitude larger compared to diabatic processes (Fig. 10 a).

The partitioning of the diabatic tendency into the contribution from different processes in Fig. 10 b shows that CRH dominates the diabatic impact until day 5. Thereafter, the contribution from total latent heating grows rapidly and becomes the dominant diabatic process. This means that much of the cloud-radiative impact operates via changes in latent heating: when CRH is included, latent heating amplifies between days 5 to 6.5, which in turn amplifies vertical motion and hence the divergent

375   flow. Following the intensification of the divergent flow, the rotational flow also increases and becomes the dominant process
at the time of cyclone maximum intensity (Fig. 10 a).
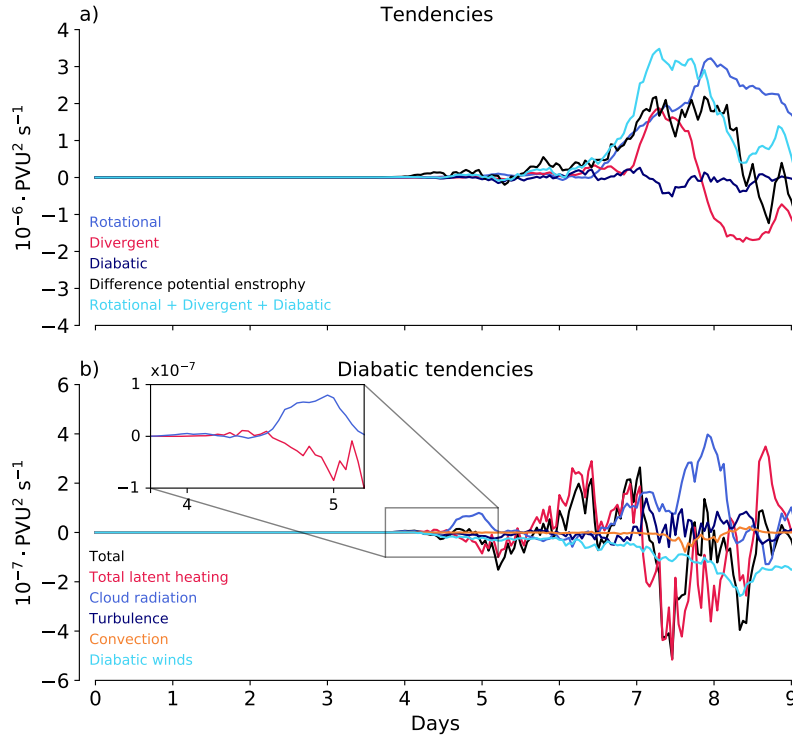
Figure 10. Evolution of the spatially integrated difference potential enstrophy tendency and contributions from individual processes diagnosed from the r.h.s. of Eq. 7. The analysis is performed around the tropopause on the 326 K isentrope. Panel (b) further decomposes the diabatic contribution into the contributions from individual diabatic processes.

The differences in near tropopause PV during the cyclone intensification thus do not result from a direct radiative increase or decrease of PV. Instead, the CRH impact seems to follow a multi-stage sequence of processes. From the absolute scale used in Fig. 10 a it is difficult to infer the contributions during the first couple of days. Therefore, and similar to Baumgart et al. (2019),

380   we also consider the relative contributions calculated as

$$\alpha = \frac{1}{\mathscr{PV}}(\mathscr{PV}_{rot/div/dia}).\tag{10}$$

Given that the only difference between the REF and the CRH simulations is the presence of cloud-radiative heating in CRH simulation, one expects that CRH initiates and dominates the differences early in the simulations. This is indeed the case. Clouds start to form at around day 2 in the lower troposphere and CRH initiates the evolution of difference potential

385   enstrophy (Fig. 11 a). However, around the tropopause on the 326 K isentrope, the differences are dominated by the divergent flow already at day 2 (Fig. 11 b). This is due to the fact that most of the early CRH occurs below the tropopause level. Thus,

the circulation responds quickly to the presence of CRH (Fig. 11) and CRH can directly impact the wind fields even in the beginning. However, the early wind changes are small and not relevant for the PV evolution during the intensification phase, as we will further investigate in Sect. 5.
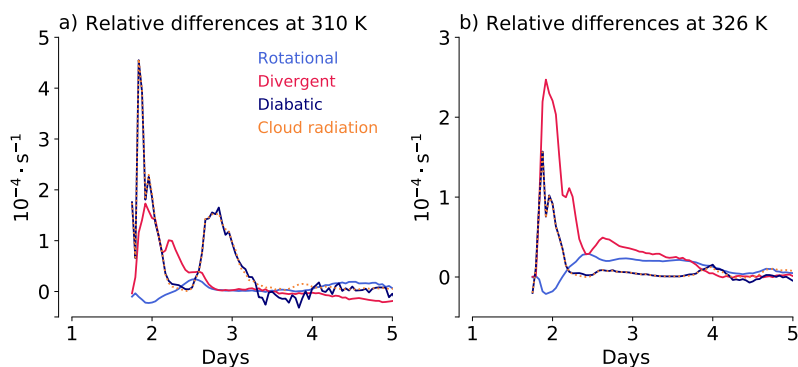
Figure 11. Contribution to the relative growth of difference potential enstrophy from the rotational and divergent flow as well as from diabatic processes as a whole and cloud-radiative heating (orange dashed line) in particular. Panel (a) is for 310 K isentrope, which is in the lower troposphere. Panel (b) is for the 326 K isentrope, which is near the tropopause.

390   An important finding of the above analysis is that much of the CRH impact occurs through changes in the total latent heating and that latent heating plays an important role in the up-scale growth of the differences between the REF and CRH cyclones. The physical mechanisms involved in the multi-stage growth to the synoptic-scale are illustrated in Fig. 12 by means of latitude-longitude plots of selected processes at different days.

At day 4, considerable differences in diabatic heating between the REF and CRH simulations occur ahead of the cyclone
395   center in the region of the warm conveyor belt. The differences are co-located with differences in precipitation (Fig. 12 a and b). This finding is consistent with our earlier finding in Fig. 4 a, which showed that CRH increases precipitation.

Following the changes in the total latent heating, vertical motion in the warm conveyor belt changes as well. The differences in vertical motion then lead to changes in near-tropopause divergence. This is demonstrated for day 5.5, for which differences from the near-tropopause divergent flow are co-located with differences in vertical motion east of the cyclone center in the
400   warm conveyor belt (Fig. 12 c,d). Finally, the CRH impact reaches the near-tropopause level, where it manifests as changes in the rotational flow that lead to a shift in the position of the trough and the ridge. This is shown for day 7.5, for which differences in the rotational flow are dominant and control the PV differences along the tropopause (Fig. 12 e and f).

5   Implications for the cyclone predictability

The multistage sequence of processes that underlies the CRH impact that we identified in Sect. 4 is very similar to the growth of
405   initial state uncertainty from the convective scale to the synoptic-scale (Baumgart et al., 2019). At the same time, however, our 2xCRH simulation with doubled cloud-radiative heating showed a substantially stronger eddy kinetic energy than the standard

CRH simulation (Fig. 3 b). Thus, the question is whether the CRH impact is the result of radiative perturbations in the early phase of the cyclone life cycle that grow in a non-linear atmosphere, or whether CRH in the later phase of the cyclone is also important. The former would mean that CRH acts as a form of initial state uncertainty; the latter would mean that CRH affects the cyclone in a continuous manner during the entire life cycle.
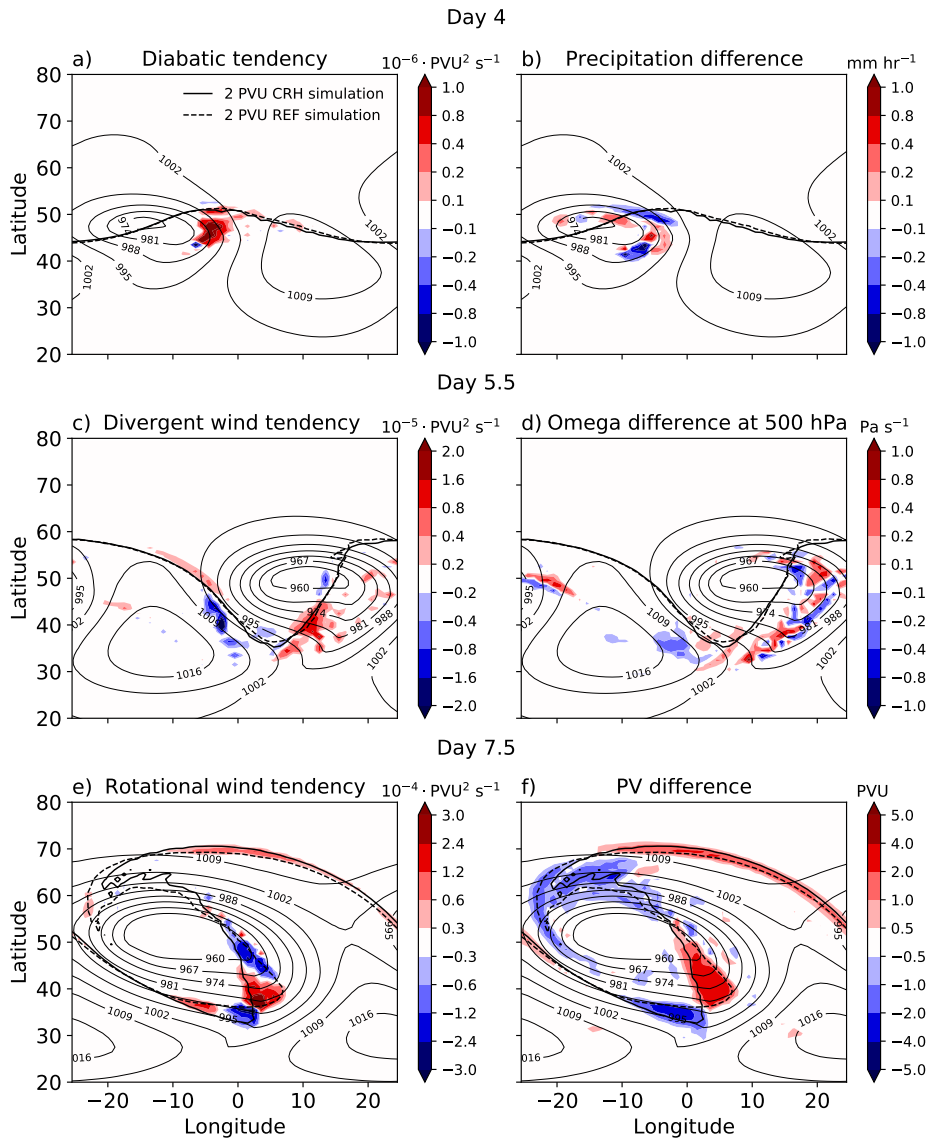
Figure 12. Illustration of the dominant contributions to the evolution of difference potential enstrophy during different stages of the cyclone growth (left). The right panel illustrates the underlying processes by means of fields that are closely related to the different contributions. Thick black contours denote the dynamical tropopause for the REF (dashed) and CRH (solid) simulations. Thin contours depict the surface pressure averaged between the two simulations.

To answer this question, we perform additional simulations in which CRH is active initially but then disabled after a certain number of days. Technically, we achieve this by restarting the model from the CRH simulation but with radiation set to zero. As a result, CRH has only interacted with the cyclone up to the restart day. We perform 4 such simulations, with CRH being deactivated at days 3, 4, 5 and 6, respectively. Fig. 13 characterizes the spatial pattern and magnitude of the temperature change due to CRH at the four days. The temperature change is averaged vertically over the depth of the troposphere.

With clouds starting to form at around day 2 (Fig. 4 b), small changes in temperature on the order of a few tenths of a Kelvin are already present at day 3 (Fig. 13 a). When restarting the simulation at this time without CRH, one can think of these temperature changes as initial perturbations. The wind has also changed to some extent at day 3 due to the presence of CRH, as can be inferred from Fig. 11. Later in the life cycle, Fig. 13 shows that the temperature change grows to values close to 1 K.
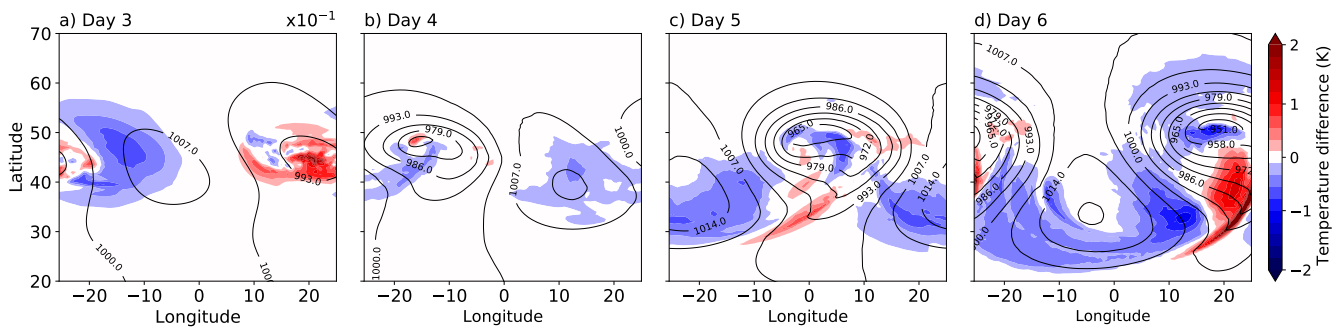
Figure 13. Temperature change due to cloud-radiative heating vertically averaged over the depth of the troposphere. The change is calculated as the temperature in the CRH simulation minus the REF simulation. Note that the scale of the temperature change at day 3 is ten times smaller than for the other days.

The new simulations make clear that CRH has a continuous impact on cyclone intensity. This is demonstrated by the evolution of eddy kinetic energy differences with respect to the CRH simulation in Fig. 14. When CRH is disabled at day 3, eddy kinetic energy closely follows the REF simulation. The temperature and wind changes induced by CRH until day 3 are thus too small to affect the cyclone in a considerable manner. It also indicates that CRH is not just affecting the cyclone by providing small initial perturbations.

When CRH is allowed to interact with the cyclone until day 4, differences in the eddy kinetic energy decrease noticeably compared to the REF simulation. When CRH is active even longer, i.e., until day 5 or 6, the evolution of eddy kinetic energy and its maximum value more and more follow the CRH simulation. It is further interesting that even when CRH is active until day 6, the cyclone does not reach the same peak intensity as when CRH is active throughout the entire life cycle.

As shown in Sect. 3 and 4, between days 3 to 5, CRH changes the latent heat release and precipitation rate (Fig. 4 a) and thus affects the near-tropopause PV through divergent flow. To check this effect further, similar to Fig. 10 we will look into the difference potential enstrophy tendencies between the REF and the new simulations (Fig. 15).
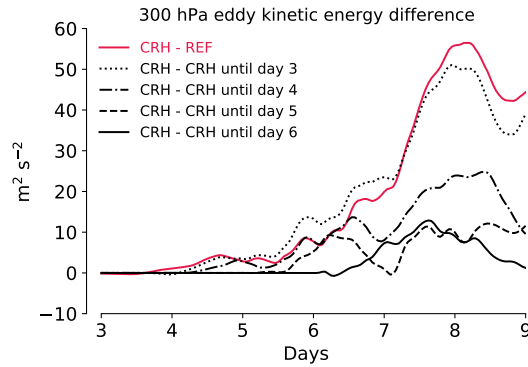
Figure 14. Evolution of eddy kinetic energy differences with respect to CRH simulation at 300 hPa for REF simulation and simulations with CRH disabled after certain days.

For the simulation starting at day 3, differences caused by CRH can still grow and change the near-tropopause PV. However, the cyclone's PV evolution is very similar to the REF simulation during the intensification phase. Differences start to appear after the cyclone reaches its maturity (Fig. 15 a). This is an indication of the non-linearity of the atmospheric flow caused by

435   the CRH in the early stages of the life cycle.
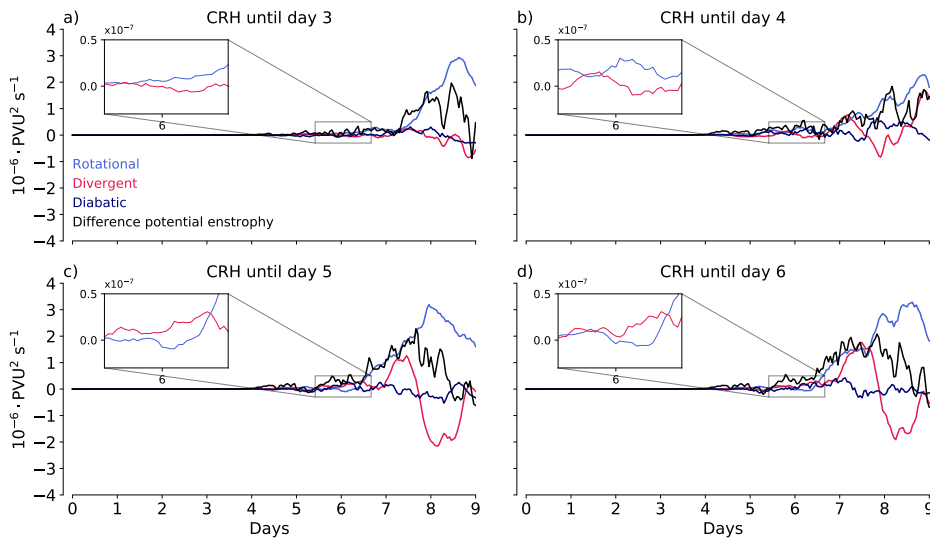
Figure 15. Similar to Fig. 10 but for tendencies calculated from the REF simulation and simulations with CRH disabled at (a) day 3, (b), day 4, (c) day 5, and (d) day 6.

Letting CRH interact with the cyclone until day 4 leads to more latent heat release and subsequently, enhances changes in the near-tropopause divergent flow. This is also evident by the enhanced different divergent wind tendencies compared to the simulation starting at day 3 (Fig. 15 b). With amplified divergent wind tendencies, differences in the rotational flow also

increase and change the near tropopause PV during the cyclone mature stage between days 6 to 7.5. This effect becomes
440   stronger if CRH is active until days 5 and 6 (Fig. 15 c and d).

There is a common pattern in the evolution of tendencies and associated processes. During the cyclone mature stage, the peak
of the divergent wind tendency is associated with differences in precipitation around day 7 which becomes stronger as long
as CRH is active in the simulations (Fig. 15). Also, there are secondary smaller peaks in the divergent wind tendencies around
day 6 which precede the marked increase in the rotational wind tendencies. The smaller peak is absent for the simulation with
445   CRH disabled at day 3 (shown by insets in Fig. 15). Thus, during the mature stage, the prominent growth of differences in the
near-tropopause PV occurs primarily due to enhanced changes in the divergent flow by CRH.

Overall, our results indicate that CRH impacts the cyclone's predictability in terms of its synoptic-scale PV evolution near
the tropopause. A small part of the CRH impact indeed is due to the non-linearity of the atmospheric flow caused by small
perturbations in the beginning. However, this effect does not change the cyclone near-tropopause PV during the mature phase.
450   In fact, it is the enhanced latent heat release and the subsequent different divergent flow by CRH that leads to changes in
near-tropopause PV. Thus, the CRH impact is important through the entire life cycle of the cyclone.

6   Conclusions

We study the impact of cloud-radiative heating (CRH) on extratropical cyclones by means of baroclinic life cycle simulations
with the ICON atmosphere model. The simulations study an idealized cyclone and are run at the high resolution of 2.5 km,
455   allowing deep convection to be modeled explicitly. In contrast to the global setup of Schäfer and Voigt (2018), we use a planar
Cartesian geometry with zonal periodic boundary conditions and we implement a new approach to isolate the impact of CRH.
An important advantage of the new approach is that it facilitates the interpretation of the CRH impact because it eliminates the
changes in the mean state due to strong clear-sky radiative cooling.

We find that CRH has a noticeable strengthening impact on the cyclone. The strengthening impact of CRH is most prominent
460   at upper levels near the tropopause, and weaker close to the surface. We also show within this idealized framework that CRH
affects the cyclone's predictability. Although our results are for a single case, we believe they allow for some general insights
into how CRH affects the growth of extratropical cyclones.

Our results are in contrast to Schäfer and Voigt (2018), who found a weakening impact of CRH. In a companion study, we
will show that this discrepancy results from differences in the ICON version and their treatment of boundary layer clouds. It
465   remains to be understood how differences in model clouds and their radiative effects result in different CRH impacts. We also
believe that further systematic studies are required to account for the role of other factors in determining the impact of CRH
on cyclones. These factors include simulations of other life cycle types, and different radiation and microphysical schemes.

Our analysis of the evolution of potential vorticity (PV) near the tropopause shows that the presence of CRH results in a
higher amplitude of the baroclinic wave and delayed cyclonic wave breaking. Both contribute to a stronger cyclone. Schäfer
470   and Voigt (2018) suggested that the reduction in the mid-tropospheric PV by CRH could be responsible for the weakening of

the cyclone. However, we show that CRH has only a small direct impact on PV. Instead, the mechanism by which CRH affects the dynamics of the cyclone operates predominantly via its influence on latent heating and near-tropopause winds.

CRH enhances total latent heat release. To elucidate the relation between CRH, increased latent heating, and near-tropopause PV, we use the PV error growth framework developed by Baumgart et al. (2018, 2019). By comparing simulations with no
475 radiation and with cloud radiation, we quantify the relative importance of diabatic and advective PV tendencies by the rotational and the divergent flows to the evolution of PV near the tropopause. We show that differences in the latent heating caused by CRH lead to differences in vertical motion in the ascending regions of the cyclone. The differences in the vertical motion then lead to changes in near-tropopause divergent flow. Following changes in the divergent flow, differences in the tropopause structure amplify with the rotational flow during the highly nonlinear stage of the baroclinic wave.

480 The multi-stage sequence of CRH impact on near-tropopause PV is similar to a previously identified mechanism of multi-stage upscale error growth that describes how convective-scale uncertainty may grow upscale to lead to changes at the synoptic-scale. However, an important result of our work is that CRH is not just affecting the cyclone by providing a kind of initial state uncertainty but that CRH has a continuous effect on the cyclone. Our results show that eddy kinetic energy amplifies as long as CRH is present in the simulation. The analysis also indicates that (synoptic-scale) perturbations to the temperature field that
485 do occur early in the simulation by CRH, do not project on differences in baroclinic growth. Instead, even in our case of a growing baroclinic wave, the most prominent growth of differences is associated with modulation of moist processes by CRH and thereafter by the nonlinear tropopause dynamics.

While the direct contribution of CRH to the cyclone PV structure is small, CRH affects the cyclone by changing cloud microphysical heating and subsequently the large-scale flow. Thus, future studies should look into the interaction between
490 radiation and cloud microphysics, and whether this interaction can play a noticeable role in numerical weather predictions of extratropical cyclones. Moreover, with models moving to storm-resolving kilometer-scale resolutions (Satoh et al., 2019), we should also consider to what extent the CRH impact might depend on an adequate representation of radiation in these models compared to low-resolution models.

Code and data availability. The ICON simulation run scripts, scripts for deriving the baroclinic life cycle initial conditions, and the analysis
495 scripts are provided in the Gitlab repository (https://gitlab.phaidra.org/climate/keshtgar-etal-cyclone-wcd2022) hosted by the University of Vienna. The simulation raw output is archived on the High-Performance Storage System at the German Climate Computing Center (DKRZ). The post-processed data used in the analysis will be published at KITopen of Karlsruhe Institute of Technology together with the Gitlab repository after the paper is accepted for publication.

Author contributions. The study was designed by AV. The implementation of the planar channel setup in ICON and the simulation design
500 were carried out by BK and AV. The ICON simulations were carried out by BK. The data analysis was done by BK with inputs from AV, CH, and MR. BK led the writing process of the manuscript, with input from all authors.

Competing interests. At least one of the (co-)authors is a member of the editorial board of Weather and Climate Dynamics

Acknowledgements. This research has been performed within project B4 of the Transregional Collaborative Research Center SFB/TRR 165 "Waves to Weather" funded by the German Research Foundation (DFG). AV received partial support from the German Ministry of Education and Research (BMBF) and FONA: Research for Sustainable Development (www.fona.de) under grant agreement 01LK1509A. We thank the German Climate Computing Center (DKRZ, Hamburg) for providing computing and storage resources as part of project 1135. The authors wish to thank Dr. Tobias Selz at LMU for providing the original code for the PV error growth diagnostic and for his feedback. We are also thankful to the developers and maintainers of the open source Python packages NumPy (Harris et al., 2020), Xarray (Hoyer and Hamman, 2017) and Matplotlib (Hunter, 2007) that were used for the data analysis.

References

Albern, N., Voigt, A., and Pinto, J. G.: Cloud-Radiative Impact on the Regional Responses of the Midlatitude Jet Streams and Storm Tracks to Global Warming, Journal of Advances in Modeling Earth Systems, 11, 1940–1958, https://doi.org/10.1029/2018MS001592, 2019.

Balasubramanian, G. and Garner, S. T.: The Role of Momentum Fluxes in Shaping the Life Cycle of a Baroclinic Wave, Journal of the Atmospheric Sciences, 54, 510 – 533, https://doi.org/10.1175/1520-0469(1997)054<0510:TROMFI>2.0.CO;2, 1997.

Barekzai, M. and Mayer, B.: Broadening of the Cloud Droplet Size Distribution due to Thermal Radiative Cooling: Turbulent Parcel Simulations, Journal of the Atmospheric Sciences, 77, 1993 – 2010, https://doi.org/10.1175/JAS-D-18-0349.1, 2020.

Baumgart, M., Riemer, M., Wirth, V., Teubler, F., and Lang, S. T.: Potential vorticity dynamics of Forecast errors: A quantitative case study, Monthly Weather Review, 146, 1405–1425, https://doi.org/10.1175/MWR-D-17-0196.1, 2018.

Baumgart, M., Ghinassi, P., Wirth, V., Selz, T., Craig, G. C., and Riemer, M.: Quantitative view on the processes governing the upscale error growth up to the planetary scale using a stochastic convection scheme, Monthly Weather Review, 147, 1713–1731, https://doi.org/10.1175/MWR-D-18-0292.1, 2019.

Bechtold, P., Jung, T., Doblas-Reyes, F., Leutbecher, M., Rodwell, M. J., Vitart, F., and Balsamo, G.: 556 Advances in Simulating Atmospheric Variability with the ECMWF model: From Synoptic to Decadal Time-scales, Tech. rep., http://www.ecmwf.int/publications/, 2008.

Booth, J. F., Wang, S., and Polvani, L.: Midlatitude storms in a moister world: Lessons from idealized baroclinic life cycle experiments, Climate Dynamics, 41, 787–802, https://doi.org/10.1007/s00382-012-1472-3, 2013.

Boutle, I. A., Beare, R. J., Belcher, S. E., Brown, A. R., and Plant, R. S.: The moist boundary layer under a mid-latitude weather system, Boundary-Layer Meteorology, 134, 367–386, https://doi.org/10.1007/s10546-009-9452-9, 2010.

Büeler, D. and Pfahl, S.: Potential Vorticity Diagnostics to Quantify Effects of Latent Heating in Extratropical Cyclones. Part I: Methodology, Journal of the Atmospheric Sciences, 74, 3567 – 3590, https://doi.org/10.1175/JAS-D-17-0041.1, 2017.

Catto, J. L.: Reviews of Geophysics Extratropical cyclone classification and its use, Reviews of Geophysics, 54, 486–520, https://doi.org/10.1002/2016RG000519.Extratropical, 2016.

Chagnon, J. M., Gray, S. L., and Methven, J.: Diabatic processes modifying potential vorticity in a north atlantic cyclone, Quarterly Journal of the Royal Meteorological Society, 139, https://doi.org/10.1002/qj.2037, 2013.

Davis, C. A., Stoelinga, M. T., and Kuo, Y.-H.: The Integrated Effect of Condensation in Numerical Simulations of Extratropical Cyclogenesis, Monthly Weather Review, 121, 2309 – 2330, https://doi.org/10.1175/1520-0493(1993)121<2309:TIEOCI>2.0.CO;2, 1993.

Doms, G., Förstner, J., Heise, E., Herzog, H.-J., Mironov, D., Raschendorfer, M., Reinhardt, T., Ritter, B., Schrodin, R., Schulz, J.-P., and Vogel, G.: A Description of the Nonhydrostatic Regional COSMO Model Part II : Physical Parameterization, Tech. rep., www.cosmo-model.org, 2011.

Ertel, H.: Ein neuer hydrodynamischer Wirbelsatz, Met. Z., 59, 277–281, 1942.

Fovell, R. G., Bu, Y. P., Corbosiero, K. L., Tung, W.-w., Cao, Y., Kuo, H.-C., Hsu, L.-h., and Su, H.: Influence of Cloud Microphysics and Radiation on Tropical Cyclone Structure and Motion, Meteorological Monographs, 56, 1–11, https://doi.org/10.1175/amsmonographs-d-15-0006.1, 2016.

Fu, Q., Krueger, S. K., and Liou, K. N.: Interactions of Radiation and Convection in Simulated Tropical Cloud Clusters, Journal of Atmospheric Sciences, 52, 1310 – 1328, https://doi.org/10.1175/1520-0469(1995)052<1310:IORACI>2.0.CO;2, 1995.

Harris, C. R., Millman, K. J., van der Walt, S. J., Gommers, R., Virtanen, P., Cournapeau, D., Wieser, E., Taylor, J., Berg, S., Smith, N. J., Kern, R., Picus, M., Hoyer, S., van Kerkwijk, M. H., Brett, M., Haldane, A., del Río, J. F., Wiebe, M., Peterson, P., Gérard-Marchant, P., Sheppard, K., Reddy, T., Weckesser, W., Abbasi, H., Gohlke, C., and Oliphant, T. E.: Array programming with NumPy, Nature, 585, 357–362, https://doi.org/10.1038/s41586-020-2649-2, 2020.

550 Hoskins, B. J., McIntyre, M. E., and Robertson, A. W.: On the use and significance of isentropic potential vorticity maps, Quarterly Journal of the Royal Meteorological Society, 111, 877–946, https://doi.org/https://doi.org/10.1002/qj.49711147002, 1985.

Hoyer, S. and Hamman, J.: xarray: N-D labeled arrays and datasets in Python, In revision, J. Open Res. Software, 2017.

Hunter, J. D.: Matplotlib: A 2D graphics environment, Computing in Science & Engineering, 9, 90–95, https://doi.org/10.1109/MCSE.2007.55, 2007.

555 Joos, H. and Forbes, R. M.: Impact of different IFS microphysics on a warm conveyor belt and the downstream flow evolution, Quarterly Journal of the Royal Meteorological Society, 142, 2727–2739, https://doi.org/10.1002/qj.2863, 2016.

Joos, H. and Wernli, H.: Influence of microphysical processes on the potential vorticity development in a warm conveyor belt: A case-study with the limited-area model COSMO, Quarterly Journal of the Royal Meteorological Society, 138, 407–418, https://doi.org/10.1002/qj.934, 2012.

560 Klinger, C. and Mayer, B.: The Neighboring Column Approximation (NCA) - A fast approach for the calculation of 3D thermal heating rates in cloud resolving models, Journal of Quantitative Spectroscopy and Radiative Transfer, 168, 17–28, https://doi.org/10.1016/j.jqsrt.2015.08.020, 2016.

Martínez-Alvarado, O., Madonna, E., Gray, S. L., and Joos, H.: A route to systematic error in forecasts of Rossby waves, Quarterly Journal of the Royal Meteorological Society, 142, 196–210, https://doi.org/https://doi.org/10.1002/qj.2645, 2016.

565 Mlawer, E. J., Taubman, S. J., Brown, P. D., Iacono, M. J., and Clough, S. A.: Radiative transfer for inhomogeneous atmospheres: RRTM, a validated correlated-k model for the longwave, Journal of Geophysical Research: Atmospheres, 102, 16 663–16 682, https://doi.org/https://doi.org/10.1029/97JD00237, 1997.

Oertel, A., Boettcher, M., Joos, H., Sprenger, M., and Wernli, H.: Potential vorticity structure of embedded convection in a warm conveyor belt and its relevance for large-scale dynamics, Weather and Climate Dynamics, 1, 127–153, https://doi.org/10.5194/wcd-1-127-2020, 570 2020.

Polvani, L. M. and Esler, J. G.: Transport and mixing of chemical air masses in idealized baroclinic life cycles, Journal of Geophysical Research Atmospheres, 112, 1–20, https://doi.org/10.1029/2007JD008555, 2007.

Raschendorfer, M.: The new turbulence parameterization of LM.COSMO Newsletter,1, 89–97, 2001.

Riemer, M. and Jones, S. C.: The downstream impact of tropical cyclones on a developing baroclinic wave in idealized scenarios of extra-575 tropical transition, Quarterly Journal of the Royal Meteorological Society, 136, 617–637, https://doi.org/https://doi.org/10.1002/qj.605, 2010.

Ruppert, J. H., Wing, A. A., Tang, X., and Duran, E. L.: The critical role of cloud-infrared radiation feedback in tropical cyclone development., Proceedings of the National Academy of Sciences of the United States of America, 117, 27 884–27 892, https://doi.org/10.1073/pnas.2013584117, 2020.

580 Saffin, L., Methven, J., and Gray, S.: The non-conservation of potential vorticity by a dynamical core compared with the effects of parametrized physical processes, Quarterly Journal of the Royal Meteorological Society, 142, 1265–1275, 2016.

Satoh, M., Stevens, B., Judt, F., Khairoutdinov, M., Lin, S.-J., Putman, W. M., and Düben, P.: Global Cloud-Resolving Models, Current Climate Change Reports, 5, 172–184, https://doi.org/10.1007/s40641-019-00131-0, 2019.

Schäfer, S. A. K. and Voigt, A.: Radiation Weakens Idealized Midlatitude Cyclones, Geophysical Research Letters, 45,
585   https://doi.org/10.1002/2017GL076726, 2018.

Schultz, D. M., Bosart, L. F., Colle, B. A., Davies, H. C., Dearden, C., Keyser, D., Martius, O., Roebber, P. J., Steenburgh, W. J., Volkert,
H., and Winters, A. C.: Extratropical Cyclones: A Century of Research on Meteorology's Centerpiece, Meteorological Monographs, 59,
1–16, https://doi.org/10.1175/amsmonographs-d-18-0015.1, 2019.

Schulzweida, U.: CDO User Guide, https://doi.org/10.5281/zenodo.3539275, 2019.

590   Spreitzer, E., Attinger, R., Boettcher, M., Forbes, R., Wernli, H., and Joos, H.: Modification of Potential Vorticity near the Tropopause by
Nonconservative Processes in the ECMWF Model, Journal of the Atmospheric Sciences, 76, 1709 – 1726, https://doi.org/10.1175/JAS-
D-18-0295.1, 2019.

Stoelinga, M. T.: A Potential Vorticity-Based Study of the Role of Diabatic Heating and Friction in a Numerically Simulated Baroclinic
Cyclone, Monthly Weather Review, 124, 849 – 874, https://doi.org/10.1175/1520-0493(1996)124<0849:APVBSO>2.0.CO;2, 1996.

595   Teubler, F. and Riemer, M.: Potential-vorticity dynamics of troughs and ridges within Rossby wave packets during a 40-year reanalysis
period, Weather and Climate Dynamics, 2, 535–559, https://doi.org/10.5194/wcd-2-535-2021, 2021.

Thorncroft, C., Hoskins, B., and McIntyre, M.: Two paradigms of baroclinic-wave life-cycle behaviour, Quarterly Journal of the Royal
Meteorological Society, 119, 17–55, 1993.

Tierney, G., Posselt, D. J., and Booth, J. F.: An examination of extratropical cyclone response to changes in baroclinicity and temperature in
600   an idealized environment, Climate Dynamics, 51, 3829–3846, https://doi.org/10.1007/s00382-018-4115-5, 2018.

Voigt, A., Albern, N., Ceppi, P., Grise, K., Li, Y., and Medeiros, B.: Clouds, radiation, and atmospheric circulation in the present-day climate
and under climate change, Wiley Interdisciplinary Reviews: Climate Change, 12, 1–22, https://doi.org/10.1002/wcc.694, 2021.

Zängl, G., Reinert, D., Rípodas, P., and Baldauf, M.: The ICON (ICOsahedral Non-hydrostatic) modelling framework of DWD and
MPI-M: Description of the non-hydrostatic dynamical core, Quarterly Journal of the Royal Meteorological Society, 141, 563–579,
605   https://doi.org/https://doi.org/10.1002/qj.2378, 2015.

Zhang, F., Bei, N., Rotunno, R., Snyder, C., and Epifanio, C. C.: Mesoscale Predictability of Moist Baroclinic Waves: Convection-
Permitting Experiments and Multistage Error Growth Dynamics, Journal of the Atmospheric Sciences, 64, 3579 – 3594,
https://doi.org/10.1175/JAS4028.1, 2007.